Experiment and modeling of an atmospheric pressure arc in an applied oscillating magnetic field

Max Karasik,[a] A. L. Roquemore, and S. J. Zweben
Princeton Plasma Physics Lab, Princeton, New Jersey 08543

A set of experiments are carried out to measure and understand the response of a free-burning atmospheric pressure carbon arc to applied transverse dc and ac magnetic fields. The arc is found to deflect parabolically for the dc field and assumes a growing sinusoidal structure for the ac field. A simple analytic two-parameter fluid model of the arc dynamics is derived, in which the arc response is governed by the arc jet originating at the cathode, with the applied $J \times B$ force balanced by inertia. Time variation of the applied field allows evaluation of the parameters individually. A fit of the model to the experimental data gives a value for the average jet speed an order of magnitude below Maecker's estimate of the maximum jet speed [H. Maecker, Z. Phys. **141**, 198 (1955)]. An example industrial application of the model is considered.   © *2000 American Institute of Physics.*
[S1070-664X(00)04406-2]

I. INTRODUCTION

Thermal plasma generators in the form of dc arcs find numerous applications in materials processing,[1] metallurgy,[2] and welding.[3] Types of arcs can be categorized by ambient pressure, arc current, and electrode geometry.[4] The interaction of various arcs with applied dc magnetic fields has been studied extensively with regard to applications such as magnetically rotated arcs, driven arcs, and magnetically balanced arcs.[5,6] In these applications, the arc is moving as a whole with respect to the surrounding atmosphere. This paper pertains to the magnetic deflection of a dc arc which is free to move on a large area anode and is fixed at an emission spot on the cathode. In this case, as will be seen below, the arc is deformed by the applied magnetic field. This type of setup is found in welding and arc furnace applications, where arc deflection due to stray magnetic fields from the electrical power feeds can cause uneven melting or furnace wall hot spots and erosion.[7–9]

Maecker[10] has given a general description of arc motion and equilibrium in external magnetic and flow fields. That description, however, becomes inadequate for high intensity arcs ($I \gtrsim 100$ A), where strong plasma flows generated by magnetic pumping effect[11] at the cathode become important. In Ref. 12, experiments on a low current ($I < 12$ A) arc subjected to an oscillating transverse magnetic field of up to 100 Hz are analyzed on the basis of a balance of the Lorentz $J \times B$ force, inertia, and aerodynamic drag. Reference 13 examined a low current arc in the dc transverse magnetic field with fixed anode and cathode regions on the basis of an inhomogeneous heat flow. Speckhofer *et al.*[14] performed experiments and three-dimensional numerical modeling on a short (3 mm) 100 A arc in the transverse dc magnetic field for a conical tungsten cathode.

A qualitative description of the behavior of an arc similar to that studied in the present paper was given in Ref. 15

for dc and 50 Hz ac applied magnetic field together with a discussion of the forces acting on the moving column of the arc. Lancaster[3] gives a description of magnetic field effects in welding, as well as empirical and analytic expressions for gas tungsten welding arc deflection in dc fields. However, no consistent quantitative experimental analysis of a high current arc motion in response magnetic fields from dc to high frequencies is found in the literature.

In addition to possible applications, development of a simple model of arc dynamics in this parameter regime should help in understanding the physical mechanisms of arc instability phenomena found in these arcs. The analysis of an arc instability occurring for certain cathode geometries in the present experiment is the subject of Ref. 16.

An important feature of the higher current arcs, such as the one in the present experiments, is a jet directed normal to the cathode surface. The jet originates at the cathode due to the increased self-magnetic field in the cathode region, where the arc is constricted due to the thermionic emission mechanism. The mechanism of the jet formation is discussed in Ref. 11. The significance of this jet in the present experiments will become apparent in Secs. IV and V below.

This paper is organized as follows: Sec. II describes the experimental setup, Sec. III gives the experimental results, Sec. IV gives a derivation of the model, Sec. V applies the model to the experimental data, Sec. VI projects the model to an industrial scale arc furnace, and finally, Sec. VII discusses the results and gives conclusions.

II. EXPERIMENTAL SETUP

A side view of the experimental setup is shown schematically in Fig. 1, and a top-down view of the setup geometry is shown in Fig. 2. The arc is struck by contact between a vertical graphite rod cathode and a flat metal surface anode whose diameter is much larger than the arc diameter. The arc length is adjusted by moving the cathode. The arc is burning at atmospheric pressure in air. Power is supplied from a current-regulated 30 kW dc power supply. Within a minute

---

[a]Present address: Naval Research Lab, Code 6731, 4555 Overlook Ave. SW, Washington, D.C. 20375. Electronic mail: karasik@this.nrl.navy.mil

2715

2716   Phys. Plasmas, Vol. 7, No. 6, June 2000

Karasik, Roquemore, and Zweben
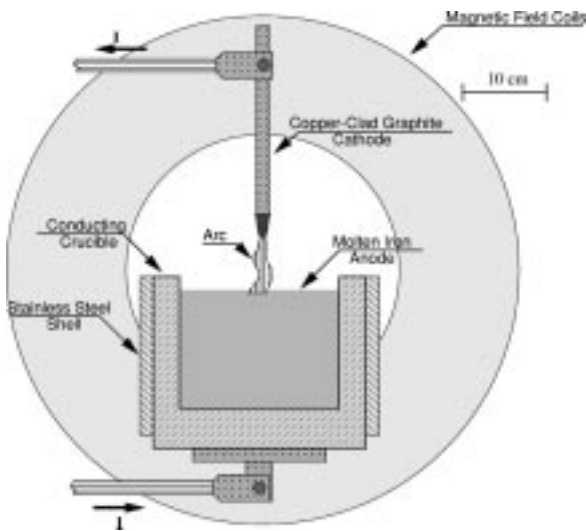
FIG. 1. Experimental setup (side view).

after the arc is initiated by an electrode contact, the metal surface of the anode becomes molten. A set of coils is used to apply a magnetic field to the arc in the direction perpendicular to the arc current. A signal generator and an audio amplifier are used to drive the coils at single frequencies in the range dc-2 kHz. Deflection experiments are conducted using the 3/8 in. copper-clad graphite rod cathode, as well as a larger 1 in. diam graphite cathode. Two different types of anodes were used; a large area iron (4 in. diam) cylinder enclosed in a conducting tar impregnated MgO brick crucible (such as used in arc furnaces), and nonmagnetic stainless steel (6 in. diam) ingots. There was no difference in the arc behavior between these two types of anodes.
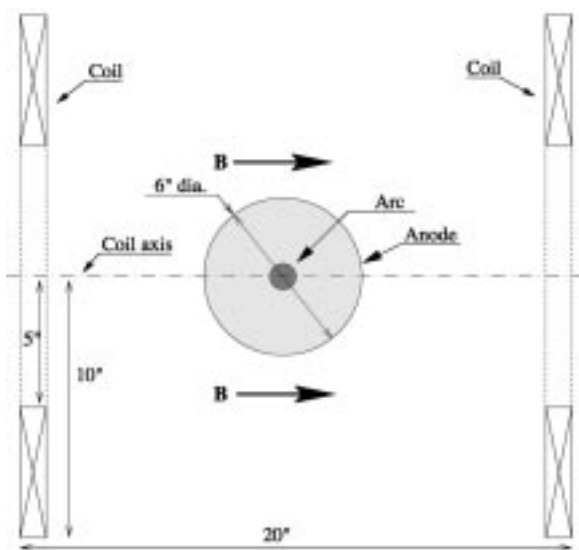
FIG. 2. Experimental setup (top down view showing the geometry of the coils for the transverse magnetic field).

The parameter space available in the experiments is arc length 0–7 cm, arc current 100–250 A, applied magnetic field strength 0–5 Gauss, and frequency dc-2 kHz.

The shape of the arc in applied magnetic field is obtained using an intensified CCD camera (ITT 4577) with typically a 10 μs gate duration at a rate of 60 frames/s. The plane of view of the camera is perpendicular to the applied magnetic field. The raw image of the arc as captured by a frame grabber is processed to give the coordinates of the points along the center of the luminous arc column by finding the centroid of brightness along each horizontal line of pixels. The arc shape is defined as the locus of such points.

Continuous monitoring of the arc column position along a horizontal line is accomplished using a linear array of 8 collimated photodiodes with a bandwidth of 80 kHz. Data acquisition is synchronized to the gating pulse of the camera.

III. DESCRIPTION OF EXPERIMENTAL RESULTS

A. Arc behavior with no external magnetic field

The starting point for all the applied transverse magnetic field experiments is an arc with less than 1% voltage and current fluctuations that is stable except for a slow precession of the arc on the tip of the cathode. The effect of this motion is that the angle the arc axis makes with the axis of the electrodes varies within approximately $\pm 5°$. Since the time scale for this precession (1 cycle in 20 s) is much longer than all other time scales in the experiment, this angle is taken as a dc position offset in the analysis below. The origin of this precession lies in thermal and erosion processes at the cathode and is discussed in Ref. 16.

B. Observed response of the arc

Motion of the arc in response to applied transverse magnetic field is strictly in the plane perpendicular to the field direction. This was ascertained by viewing the arc directly as well as at 90° using a mirror.

No significant differences in the response of the arc are found between 3/8 and 1 in. diam graphite cathodes and between iron and steel anodes.

1. dc and low frequencies

For dc applied magnetic field, the arc exhibits a deflection in the direction expected from the $\mathbf{J} \times \mathbf{B}$ force, with maximum deflection at the anode (Fig. 3). The shape of the deflected arc is stable and is well fitted by a parabola. For low frequency oscillating transverse magnetic field, when the applied frequency is $\lesssim 80$ Hz, the arc is swept across the anode surface while being anchored at the cathode. The shape of the arc at any point in time is parabolic, as in the dc field case. The amount of deflection and the arc shape are found to be independent of magnetic field frequency for low frequencies. This can seen in Fig. 4 showing the results of parabolic fit to arc shape vs frequency.

Figure 4 is obtained by fitting a parabola $\xi(z) = A_1 z + A_2 z^2$, where z is the vertical distance from the cathode and ξ is the measured displacement from the vertical, to the arc shape for different frequencies of the applied field. The coefficient A_1 accounts for the variation of the angle of the arc
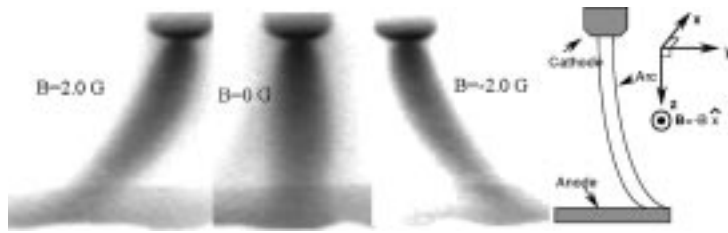
FIG. 3. Arc deflection for dc and low frequency ac magnetic field. Pictures are negatives of images taken with 10 μs exposure intensified CCD camera. Pictures are compressed vertically 2.4:1. The schematic shows the location of the cathode and the anode and the direction of applied magnetic field.

with respect to the vertical (discussed in Sec. III A above). For each frequency, the fits are done at several different phases of the applied magnetic field. The resulting A_2 coefficients vary linearly with the instantaneous applied magnetic field. Effects of any dc bias magnetic field, such as due to Earth's magnetic field and the field from the current feeds, are removed by performing a linear fit of A_2 vs the instantaneous applied magnetic field. Each data point in Fig. 4 is the mean value of the slope thus obtained.

2. High frequencies

For applied magnetic field frequencies above 100 Hz, the arc shape is no longer parabolic. As in low frequency case, the arc is anchored at the cathode and is swept across a line segment of the anode. However, the arc shape at any moment in time is a growing sinusoid, with the amplitude increasing towards the anode. Sample images of the arc at three different frequencies of applied field are shown in Fig. 5(a). The longitudinal mode number increases with the applied frequency, while the amplitude of displacement at a given vertical position decreases with increasing frequency. For higher arc currents, the mode number decreases. Time evolution of the arc shape for fixed experimental conditions is shown in Fig. 5(b). The arc shape is periodic in time at the frequency of the applied field. The analysis of the high frequency data are in Sec. V B.

IV. THEORETICAL MODEL

The arc shape data for dc and ac applied magnetic fields was quantitatively analyzed on the basis of a model derived below. Comparison of data with the model is given in Sec. V.

A. Assumptions

In order to make an analytical solution tractable, a one-dimensional (1D), linear approximation is used. The following assumptions are made in the derivation:

(1) Arc dynamics can be described by single fluid equations due to the high collisionality, as discussed in Sec. IV G.
(2) A thin-wire (1D) approximation is made replacing actual cross-sectional profiles of mass density, current density, and axial flow velocity with linear mass density, arc current, and an average jet speed, respectively. The linear mass density and average jet speed are assumed constant along the length of the column. Any pressure gradients are assumed to be internal to the arc. The assumption of constant average jet speed is probably reasonable because, even though the peak velocity decreases some-

what with distance from the cathode, the velocity averaged over the arc cross section should remain fairly constant due to momentum conservation in the jet. This can be seen in the time evolution of the arc shape in Fig. 5(b), where the "bends" in the arc column are moving down at an approximately constant rate.
(3) The arc displacement from the equilibrium axis is sufficiently small for transverse component of current density and jet velocity to be small compared to the respective axial components.
(4) Motion of the arc due to heat flux effects[17] is negligible (see Sec. IV G).
(5) The self-magnetic field effect is negligible. This assumption is relaxed in Sec. IV E.
(6) The arc is anchored at the cathode emission spot and is free to move over the anode surface. This assumption is relaxed in Sec. IV C.
(7) Gravity effects are neglected. The characteristic flow speed due to buoyancy is $\sqrt{gL}\sim0.8$ m/s, where g is acceleration of gravity and $L\leqslant0.07$ m is the arc length; it is much slower than the average jet speeds inferred (~20 m/s).
(8) The applied magnetic field is uniform along the length of the arc. This assumption is examined in Sec. IV F.

B. Derivation of the equation of the arc shape

With the above assumptions, the force balance equation is
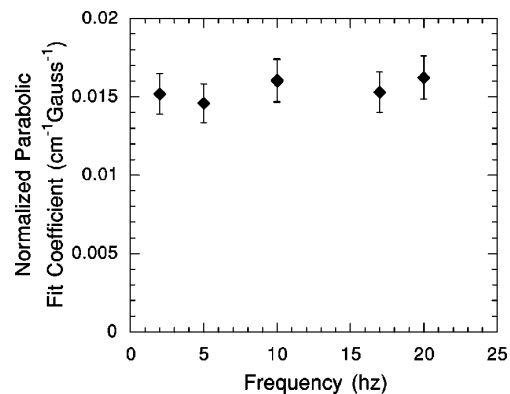
FIG. 4. The shape of the arc is independent of frequency for low frequency applied magnetic field. Here, the coefficient A_2 resulting from the fit of a parabola $\xi(z)=A_1z+A_2z^2$, where z is the vertical distance from the cathode, to the arc shape, normalized to instantaneous magnetic field is plotted vs frequency. Arc current is 145 A; arc length is 4 cm. The error bars are the standard error from linear fits of data at different phases of the applied field.
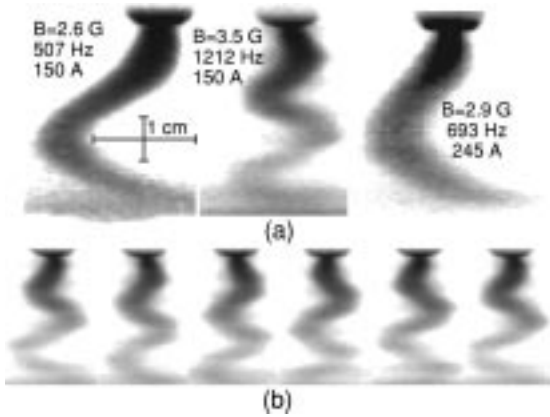
FIG. 5. (a) Sample pictures of the arc in applied ac magnetic field. The geometry is the same as in Fig. 3. Labels indicate the peak amplitude and frequency of applied magnetic field and the arc current. As can be seen from the pictures, the mode number is higher for higher frequency and lower for higher current. (b) Time evolution of the arc shape for 3.5 G 1212 Hz applied magnetic field and 150 A arc current. The pictures are consecutive frames taken at 60 frames/s. The beat frequency between the applied field frequency and the framing rate is 12 Hz, resulting in the arc shape repeating itself every five frames. All pictures are negatives, 10 μs exposure; horizontal scale is expanded 2.4:1.

$$m\frac{\partial \boldsymbol{v}}{\partial t} + m(\mathbf{v}\cdot\nabla)\mathbf{v} = \boldsymbol{I}\times\boldsymbol{B}, \tag{1}$$

where m is the linear mass density. Letting z-axis be the equilibrium arc axis, $\boldsymbol{B}=\hat{x}B\cos(\omega t)$, jet velocity $\boldsymbol{v}=\tilde{v}\hat{y}+v\hat{z}$, where v is the jet speed and $\tilde{v}$ is the perturbed transverse velocity, with $\tilde{v}/v \ll 1$. Linearizing Eq. (1) in this way, get

$$\frac{\partial \tilde{v}}{\partial t} + v\frac{\partial \tilde{v}}{\partial z} = \frac{IB}{m}\cos(\omega t). \tag{2}$$

Letting ξ denote transverse displacement, $\tilde{v}$ is given by the convective derivative $\tilde{v}=D\xi/dt$. Expanding the convective derivative and linearizing we get

$$\tilde{v} = \frac{\partial \xi}{\partial t} + v\frac{\partial \xi}{\partial z}. \tag{3}$$

Substituting Eq. (3) into Eq. (2), we obtain

$$\frac{\partial^2 \xi}{\partial t^2} + 2v\frac{\partial^2 \xi}{\partial t\partial z} + v^2\frac{\partial^2 \xi}{\partial z^2} = \frac{IB}{m}\cos(\omega t). \tag{4}$$

The initial conditions at the cathode $z=0$ corresponding to the assumption that the arc is fixed at the cathode emission spot are $\xi(z,t)|_{z=0}=0$ and $\partial\xi/\partial z|_{z=0}=0$. Since we seek a steady-state solution in time with initial conditions in z, Eq. (4) can be solved by Fourier transforming in time and Laplace transforming in space (along z). One gets

$$\xi(z,t) = \frac{IB}{m\omega^2}\left[\cos\left(\omega t - \frac{\omega z}{v}\right)\right.$$
$$\left. -\cos(\omega t) - \frac{z\omega}{v}\sin\left(\omega t - \frac{\omega z}{v}\right)\right]. \tag{5}$$
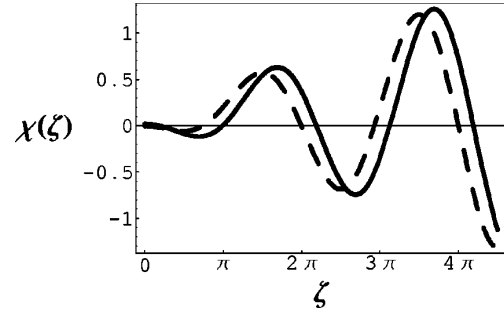
FIG. 6. Derived arc shape and its time evolution: dashed curve shows arc shape at a particular time τ_1, solid—a short time $\Delta\tau$ later. In this example, $\tau_1=0$, $\Delta\tau=0.6$, $M=-0.1$. Cathode is at (0,0). See text for definition of the dimensionless variables and numbers.

For $(\omega z/v)\ll 1$ (low frequency limit), sin and cos can be expanded in power series, giving

$$\xi(z,t) = \frac{IB\cos(\omega t)}{2mv^2}z^2 + \frac{IB\omega\sin(\omega t)}{3mv^3}z^3 + \mathcal{O}\left(\frac{z\omega}{v}\right)^4 \tag{6}$$

which gives parabolic deflection plus a cubic correction that is important for zero crossings of the magnetic field (when phase ωt is a multiple of $\pi/2$). For the dc magnetic field, in the limit $\omega\to 0$, Eq. (6) reduces to

$$\xi(z,t) = \frac{IB}{2mv^2}z^2. \tag{7}$$

Parabolic deflection is thus recovered in the low frequency limit, as expected from the experiments described in Sec. III B.

Equation (7) is consistent with the expression for dc deflection given in Ref. 3,

$$y = \frac{JBz^2}{2\rho v^2}, \tag{8}$$

where J and ρ are current and mass densities, respectively. Assuming J and ρ to be average values over the arc cross section and multiplying top and bottom of Eq. (8) by the cross-sectional area of the arc, one arrives at Eq. (7).

The above equations can be rewritten in dimensionless form by defining a length scale by v/ω, equal to the distance the jet travels in an oscillation of the applied field, divided by 2π; the time scale by $1/\omega$, equal the oscillation period divided by 2π. Equation (5) can then be rewritten as

$$\chi(\zeta,\tau) = M[\cos(\tau-\zeta) - \cos(\tau) - \zeta\sin(\tau-\zeta)], \tag{9}$$

where $\chi \equiv \xi\omega/v$, $\tau \equiv \omega t$, $M \equiv IB/m\omega v$, and $\zeta \equiv z\omega/v$. The dimensionless number M, rewritten as $M=(IB/\omega)/mv$ can be interpreted as the ratio of transverse momentum imparted by the $\boldsymbol{I}\times\boldsymbol{B}$ force on a section of the arc in a time $1/\omega$ to the axial momentum of the jet.

Equation (9) is plotted in Fig. 6 for a particular time τ and a short time $\Delta\tau$ later. As can be seen in the figure, the fluid elements of the arc move mostly in the axial direction away from the cathode. The same can be seen in the experimentally observed time evolution of the arc shape [Fig.

5(b)]. The fluid elements thus do not cross the axis with each oscillation of the applied magnetic field, and the spatially oscillatory arc shape results mostly from the switching of the initial parabolic deflection of each fluid element near the cathode ($\zeta \ll 1$).

Figure 7 zooms in on region $\zeta \ll 1$, which represents the cases of low frequency, high jet speed, or short distances from the cathode. In Fig. 8, $\chi(\zeta, \tau)$ is plotted for many values of τ, showing the expected envelope for arc displacement. The envelope can be defined as the locus of peaks of χ, i.e., (ζ, χ) such that $\partial \chi / \partial \zeta = 0$. Applying this condition to Eq. (9), one gets

$$\chi|_{(\partial \chi / \partial \zeta)=0} = \pm M[\zeta - \sin \zeta]. \tag{10}$$

Or, for $\zeta \gg 1$,

$$\chi|_{(\partial \chi / \partial \zeta)=0} \approx \pm M \zeta. \tag{11}$$

That is, the envelope for arc motion is approximately a cone. The above equations are shown in Fig. 8 as gray and broken lines, respectively.

C. Effect of the cathode spot motion

If the assumption of arc attachment spot being immobile on the cathode is relaxed, the arc shape, and therefore quantities inferred from it could change. The effect would depend on how much and how quickly the spot would move in response to the applied transverse field. Assuming the spot would move in the plane of motion of the arc column (transverse to the applied field), and that the surface of the cathode is flat and parallel to the anode surface, let the position of the spot on the cathode be given as $y = f(t)$. If the other assumptions made in the above derivation of arc shape (Sec. IV A) are retained, the differential equation (4) for arc shape still holds. The only change is that the initial conditions at the cathode $z = 0$ are now a function of time, $\xi(z,t)|_{z=0} = f(t)$ and $(\partial \xi / \partial z)|_{z=0} = 0$. Incorporating these initial conditions in Laplace transform in z, the solution, rewritten in the same dimensionless form as Eq. (9), becomes

$$\chi(\zeta, \tau) = \frac{\omega}{v} [f(\tau - \zeta) + \zeta f'(\tau - \zeta)]$$

$$+ M[\cos(\tau - \zeta) - \cos(\tau) - \zeta \sin(\tau - \zeta)]. \tag{12}$$
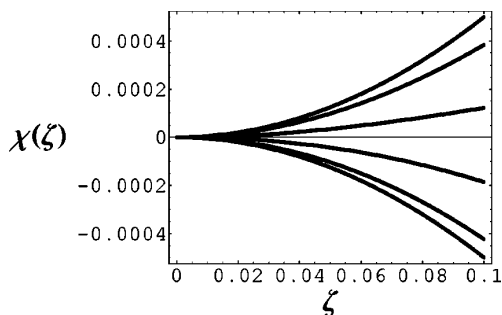
FIG. 7. Arc shape for $\zeta \ll 1$ for several different times. $M = -0.1$. Cathode is at (0,0).
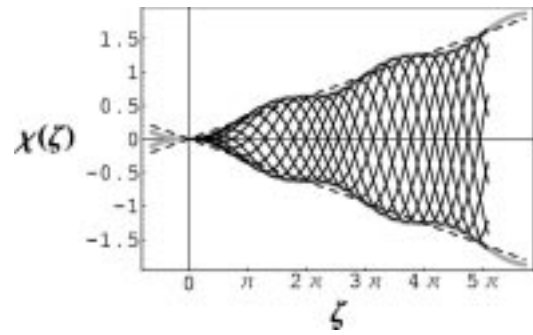
FIG. 8. Overlay of arc shapes at different times shows the envelope of the arc displacement. The envelope for arc motion, given by $\pm M[\zeta - \sin(\zeta)]$, is shown in light gray. A cone given by lines $\pm M \zeta$ is shown dashed. Here, $M = -0.1$. Cathode is at (0,0).

If, furthermore, the spot is assumed to move harmonically and in phase with the driving field, with an amplitude a, $f(t) = a \cos(\omega t)$, arc shape becomes

$$\chi(\zeta, \tau) = \left(M + \frac{a\omega}{v} \right) [\cos(\tau - \zeta) - \cos(\tau) - \zeta \sin(\tau - \zeta)]$$

$$+ \frac{a\omega}{v} \cos(\tau). \tag{13}$$

The shape of the arc in this case is thus identical to the anchored spot case, except for an increase in the amplitude of arc displacement $M \rightarrow M + a\omega / v$ and a harmonic motion of the column as a whole.

D. Aerodynamic drag

In the above derivation the effect of the force of drag of the surrounding gas on the moving arc was neglected. The hydrodynamic Reynolds number for transverse motion of the arc is

$$\text{Re} = \frac{Lv\rho}{\eta} \sim \frac{(0.01 \text{ m})(1 \text{ m/s})(0.07 \text{ kg/m}^3)}{1.3 \times 10^{-4} \text{ kg/m s}} \sim 5, \tag{14}$$

where L is the arc diameter; ρ and η are mass density and viscosity of the surrounding gas, respectively, and their values are taken from Ref. 18. Since Re is low, the aerodynamic drag per unit length of the column experienced by the arc as it moves through the surrounding gas is proportional to speed,[19]

$$F_{\text{drag}} = C \eta v, \tag{15}$$

where $C \sim 1$ is a dimensionless constant. In the above, the relevant v is the component of velocity normal to the arc column, and, for $\partial \xi / \partial z \ll 1$ it is $\partial \xi / \partial t$. Adding this force term to the equation for arc shape, we get, in dimensionless form,

$$\frac{\partial^2 \chi}{\partial \tau^2} + 2 \frac{\partial^2 \chi}{\partial \tau \partial \zeta} + \frac{\partial^2 \chi}{\partial \zeta^2} = M \cos(\tau) - G \frac{\partial \chi}{\partial \tau}, \tag{16}$$

where $G \equiv C \eta / m \omega$, the other quantities defined as before. Equation (16) can be solved analytically using the same
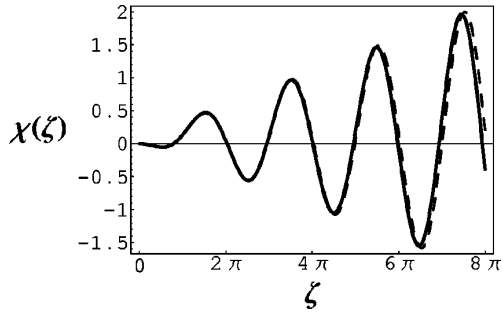
FIG. 9. Arc shape with (solid line) and without (dashed) the aerodynamic drag effect. $M = -0.081$, $G = 2.8 \times 10^{-3}$, frequency of applied magnetic field is 1212 Hz. At this frequency, a 4 cm arc extends to $\zeta \approx 4\pi$, and the drag effect is thus negligible.
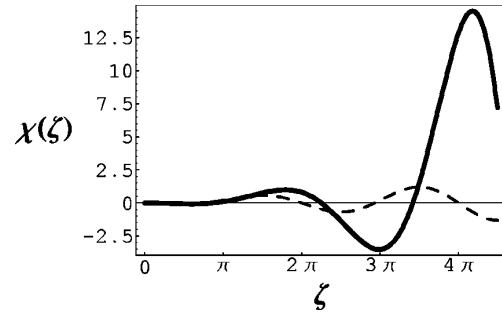
FIG. 10. Calculated shape of the arc including the self-magnetic field effect. $K = \sqrt{N} = 0.44$, $M = -0.1$. For comparison, the shape calculated without the self-field effect ($K = 0$) is shown as the dashed curve. At 1200 Hz, a 4 cm long arc extends to $\zeta \approx 4\pi$.

Fourier/Laplace method as before. The result shows that the effect of drag is small for $\zeta\sqrt{G} \ll 1$, i.e., for $z \ll v\sqrt{m/C\eta\omega} \sim 5$ cm for the highest frequencies studied. For lower frequencies, the effect is negligible even for longer arc lengths. Figure 9 shows an example of the arc shape with and without the aerodynamic drag effect for parameters corresponding to the high frequency experiments.

E. Effect of the self-magnetic field

In this section, an attempt is made to relax the assumption made until now of neglecting the self-magnetic field effect in deriving the shape of the arc. Still following the 1D approximation, the local effect of the self-field on a displaced arc column can be modeled as a force per unit length of the column dependent on the local curvature of the column and normal to it,[20]

$$F_{\text{self}} = \frac{\mu_0 I^2}{4\pi R} \ln\frac{l}{a}, \tag{17}$$

where I is the arc current, R is local radius of curvature, a is the radius of arc column, and l is a characteristic length of the bending including geometrical factors. The force balance equation is then given by

$$m\frac{\partial \boldsymbol{v}}{\partial t} + m(\mathbf{v}\cdot\nabla)\mathbf{v} = \boldsymbol{I}\times\boldsymbol{B} + \boldsymbol{F}_{\text{self}}, \tag{18}$$

where m is mass per unit length of arc, I is arc current. Proceeding as in Sec. IV B, get

$$\frac{\partial^2 \xi}{\partial t^2} + 2v\frac{\partial^2 \xi}{\partial t\partial z} + v^2\frac{\partial^2 \xi}{\partial z^2} = \frac{IB}{m}\cos(\omega t) + \frac{F_{\text{self}}}{m}. \tag{19}$$

For sufficiently small slope of the displaced arc column, the curvature can be approximated by the second derivative of the displacement,[21] $1/R \approx -(\partial^2 \xi/\partial z^2)$, where the minus sign is included to indicate the outward direction of the self-field force. Substituting expression (17) and making this approximation, the equation for arc displacement becomes

$$\frac{\partial^2 \xi}{\partial t^2} + 2v\frac{\partial^2 \xi}{\partial t\partial z} + \left[v^2 + \frac{\mu_0 I^2}{4\pi m}\ln\frac{l}{a}\right]\frac{\partial^2 \xi}{\partial z^2} = \frac{IB}{m}\cos(\omega t). \tag{20}$$

Rewriting this in dimensionless form,

$$\frac{\partial^2 \chi}{\partial \tau^2} + 2\frac{\partial^2 \chi}{\partial \tau\partial \zeta} + (1+N)\frac{\partial^2 \chi}{\partial \zeta^2} = M\cos(\tau), \tag{21}$$

where $N \equiv (\mu_0 I^2/4\pi mv^2)\ln(l/a)$, the other dimensionless variables and M defined as before. The dimensionless quantity N rewritten as $F_{\text{self}}/(mv^2/R)$ using Eq. (17), can be seen as the ratio of the self-field force to the centripetal force of the jet. Another interpretation of N is the ratio of the magnetic energy to the kinetic energy in the jet, $\mu_0 I^2/4\pi mv^2 = [(B_{\text{self}}^2/2\mu_0)\pi a^2]/(mv^2/2)$, where $B_{\text{self}} = \mu_0 I/2\pi a$ is the self-field at arc radius a and $B_{\text{self}}^2/2\mu_0$ is the magnetic energy density.

Since N is dependent on l only logarithmically, it is taken as a constant. Using the initial conditions and the method used in Sec. IV B, the solution is

$$\chi(\zeta,\tau) = M\left[\cos\left(\tau - \frac{\zeta}{1+K^2}\right)\cosh\left(\frac{K\zeta}{1+K^2}\right)\right.$$
$$\left. -\frac{1}{K}\sin\left(\tau - \frac{\zeta}{1+K^2}\right)\sinh\left(\frac{K\zeta}{1+K^2}\right) - \cos(\tau)\right], \tag{22}$$

where $K \equiv \sqrt{N}$.

In the limit $K \to 0$, Eq. (22), as expected, reduces to the arc shape with no self-field effect, given by Eq. (9). For sufficiently high applied magnetic field frequency when $K\zeta \gtrsim 1$, even if $K < 1$, a significant effect is expected because of exponential growth of cosh and sinh. The arc shape given by Eq. (22) is plotted in Fig. 10 for a value of K consistent with the experimental arc parameters. The arc shape without including the self-magnetic field effect is also shown for comparison. Clearly, inclusion of the self-field interaction in this manner dramatically affects the calculated arc shape for $\zeta > 1/K$. The envelope of arc displacement no longer grows linearly with distance from the cathode, as in Fig. 8, but grows exponentially. The perturbation given to the arc shape by the oscillating applied field is then growing with a mechanism similar to the $m = 1$ instability in a z-pinch.[22]

In the low frequency and dc limit for which $\zeta \ll 1$, Eq. (22) can be expanded as

$$\chi = \frac{M}{1+K^2}\left[\frac{1}{2}\cos(\tau)\zeta^2 + \frac{\sin(\tau)}{3(1+K^2)}\zeta^3\right] + \mathcal{O}(\zeta^4). \quad (23)$$

The deflection is thus still parabolic to the lowest order, with the self-field contribution that is small for $K < 1$. For $K \gtrsim 1$ however, the arc would be deflected less than expected without inclusion of self-field effect [compare to Eq. (6)].

Going back to dimensional quantities, the deflection in the dc ($\omega \to 0$) limit becomes

$$\xi(z) = \frac{IB}{2mv^2(1+N)}z^2, \quad (24)$$

where $N = K^2$ as before.

The numerical value of N depends on the geometry of the deformed arc column. For parabolically deflected column, N is given by (see the Appendix)

$$N = \frac{\mu_0 I^2}{4\pi m v^2}\left(\ln\frac{h}{a} - 1\right), \quad (25)$$

where h is the electrode separation, and a is the arc radius. For nonparabolic (higher frequency) deflection, a numerical calculation discussed in the Appendix shows that Eq. (17) gives an overestimate for the self-field effect. The effect of self-fields in the experiment is discussed in Sec. V C.

F. Nonuniform applied magnetic field

It has been assumed until now that the applied magnetic field is uniform over the length of the arc. If a gradient exists in the applied field, the driving term on the right-hand side of Eq. (4) will be a function of z. Assuming the applied field decreases form a value B at the cathode ($z = 0$) to a value B_a at the anode ($z = h$),

$$B(z) = \frac{(B_a - B)z}{h} + B. \quad (26)$$

Substituting this $B(z)$ into the driving term on the right-hand side of Eq. (4), and rewriting in dimensionless form, we obtain this modified equation for arc shape,

$$\frac{\partial^2\chi}{\partial\tau^2} + 2\frac{\partial^2\chi}{\partial\tau\partial\zeta} + \frac{\partial^2\chi}{\partial\zeta^2} = M\cos(\tau)\left((b-1)\frac{\zeta v}{h\omega} + 1\right), \quad (27)$$

where $b \equiv B_a/B$. Using the same method as above, the solution is

$$\chi(\zeta,\tau) = M[\cos(\tau-\zeta) - \cos(\tau) - \zeta\sin(\tau-\zeta)]$$
$$+ \frac{Mv(b-1)}{h\omega}[2\sin(\tau) - 2\sin(\tau-\zeta)$$
$$- \zeta\cos(\tau) - \zeta\cos(\tau-\zeta)], \quad (28)$$

where the quantity in the first square brackets is the original solution for a uniform field. The ratio of magnitudes of the correction to the original solution is $(b-1)v/h\omega$. The correction is therefore small for $v/h\omega \ll 1$, or $\omega \gg v/h$, even if the magnetic field decreases to 0 at the anode ($b = 0$). In the

present experiment, $v \sim 23$ m/s and $h \sim 0.04$ m. Thus, for frequencies greater than ≈ 100 Hz, the correction due to an applied field gradient can be ignored.

For low frequencies, when $v/h\omega \gtrsim 1$, Eq. (28) can be expanded in powers of ζ as before, since in this limit $\zeta = z\omega/v \leqslant h\omega/v < 1$,

$$\chi = \frac{M}{2}\cos(\tau)\zeta^2 + M\left(\frac{1}{3}\sin(\tau) - \frac{(1-b)v\cos(\tau)}{6h\omega}\right)\zeta^3 + \mathcal{O}(\zeta)^4. \quad (29)$$

The largest difference in the arc shape due to nonuniformity would then occur at the anode, i.e., at $\zeta = h\omega/v$. The ratio of the third term to the first one would then equal $(1-b)/3$. Thus the error in assuming a uniform applied field is $(1-b)/3 \times 100\%$. Measurements of the applied magnetic field in the present experiments show a maximum gradient of 20% over the 4 cm arc length, corresponding to $b = 0.8$ and therefore the maximum error in neglecting the gradient is 7%.

G. Range of validity of the model

The validity of the derived model is limited by the assumptions listed in Sec. IV A. The high collisionality assumption is justified since the collision frequency is greater than the cyclotron frequencies and the applied field frequency, $\tau_{ee} \sim \tau_{en} \sim 10^{11}$ Hz. $\tau_{ce} \sim 2.8 \times 10^6 B$ Hz$\sim 10^8$ Hz,[23] and the highest applied field frequency is 2 kHz.

Assumption (3) is examined as follows. The arc current direction is always tangent to the arc column. Unit tangent vector to a curve $r(t) = x(t)\hat{x} + y(t)\hat{y} + z(t)\hat{z}$ is given by $T = r'(t)/\|r'(t)\|$. Parameterizing the arc shape by the distance from cathode z, we get

$$r(z) = z\hat{z} + \xi(z)\hat{y},$$
$$r'(z) = \hat{z} + \frac{\partial\xi}{\partial z}\hat{y}. \quad (30)$$

From Eq. (5),

$$\frac{\partial\xi}{\partial z} = \frac{M\omega z}{v}\cos\left(\omega t - \frac{\omega z}{v}\right). \quad (31)$$

The direction of the arc current is then given by

$$T = \frac{\hat{z} + \hat{y}\dfrac{M\omega z}{v}\cos\left(\omega t - \dfrac{\omega z}{v}\right)}{\sqrt{1 + \left(\dfrac{M\omega z}{v}\right)^2\cos^2\left(\omega t - \dfrac{\omega z}{v}\right)}}. \quad (32)$$

Therefore, the transverse component of the current is small for $M\omega z/v \ll 1$, i.e., $z \ll mv^2/IB$. From the experiment, $mv^2/IB \approx 4$ cm at 5.6 G and 150 A. Thus, the assumption of small transverse current component is valid for distances from the cathode up to 4 cm; further for smaller applied fields and higher arc currents (if $v \propto I$ as found in the present experiments, see Sec. V B).

The transverse component of velocity $\tilde{v}$ can be compared to the axial jet speed v by evaluating $\tilde{v}$ using definition (3) and Eq. (5),

2722   Phys. Plasmas, Vol. 7, No. 6, June 2000

Karasik, Roquemore, and Zweben

$$\frac{\tilde{v}}{v} = M\left[\sin(\omega t) - \sin\left(\omega t - \frac{\omega z}{v}\right)\right].\tag{33}$$

Thus, $\tilde{v}$ is small for $M \ll 1$, which is always the case in the present experiments ($M \lesssim 0.3$). For $\omega \to 0$ (dc deflection case), Eq. (33) becomes $\tilde{v}/v = M(\omega z/v)$, or $\tilde{v}/v = IBz/mv^2$, and the condition for validity is then the same as derived above, namely, $z \ll mv^2/IB$, or $z < 4$ cm.

Assumption (4) can be verified by considering the displacement due to anisotropic heat flux in a curved arc column. This effect is discussed in Ref. 17, where the following expression is derived for the velocity of the arc temperature distribution:

$$v_T \approx 10 d_m\left(\frac{\rho_m}{\rho_e}\right)\left(\frac{1}{R}\right),\tag{34}$$

where d_m is thermal diffusivity, ρ is mass density, R is the radius of curvature of the column, and subscripts m and e refer to values at the temperature maximum in the arc and externally to the arc, respectively. The direction of this motion is towards the center of curvature. In order estimate the importance of this effect, the displacement ξ' caused by v_T over the transit time of the jet from the cathode to the anode can be compared to the displacement ξ derived above neglecting this effect. From Eq. (9) the curvature is

$$\frac{1}{R} = \frac{\partial^2 \xi}{\partial z^2} = \frac{\omega}{v}\frac{\partial^2 \chi}{\partial \zeta^2}$$
$$= \frac{\omega M}{v}[\cos(\tau - \zeta) + \zeta \sin(\tau - \zeta)] \sim \frac{\omega M}{v}\zeta;\tag{35}$$

v_T therefore is

$$v_T \sim 10 d_m\left(\frac{\rho_m}{\rho_e}\right)\left(\frac{Mz\omega^2}{v^2}\right).\tag{36}$$

The displacement due to v_T would then be

$$\xi' = \int_0^t v_T dt = \int_0^z \frac{v_T}{v}dz = 10 d_m\left(\frac{\rho_m}{\rho_e}\right)\left(\frac{M\omega^2 z^2}{2v^3}\right).\tag{37}$$

Using the envelope of arc displacement Eq. (11), $\xi \sim Mz$ and therefore

$$\frac{\xi'}{\xi} = 10 d_m\left(\frac{\rho_m}{\rho_e}\right)\left(\frac{\omega^2 z}{2v^3}\right).\tag{38}$$

For this effect to be small, ξ'/ξ should be $\ll 1$. From Eq. (38), this implies

$$z \ll \left(\frac{v^3}{\omega^2}\right)\left(\frac{\rho_e}{5\rho_m d_m}\right)$$
$$\approx \frac{(23\ \text{m/s})(0.7\ \text{kg/m}^3)}{((2\pi)1200\ \text{Hz})^2(5)(1.7\times10^{-2}\ \text{kg/m}^3)(0.02\ \text{m}^2/\text{s})}$$
$$= 0.09\ \text{m},\tag{39}$$

where density and diffusivity values are taken from Ref. 18. Thus, Assumption (4) is valid for $z \ll 9$ cm for $f \lesssim 1200$ Hz

and $v \approx 20$ m/s, which is the case for the present experiments. For frequencies lower than 1200 Hz and for higher jet speeds, the effect is negligible even for longer arc lengths.

V. APPLICATION OF THE MODEL TO EXPERIMENT

In this section, the above model is applied to the experimental results. The model for arc shape has two parameters that are not measured directly in the experiments; the axial jet speed v and the linear mass density m. For dc and low frequency deflection, both of these parameters appear in a single coefficient [see Eq. (7)] that can be obtained from the parabolic fit but cannot be evaluated separately. For higher frequencies ($\omega z/v \gtrsim 1$), the jet speed and mass density appear as independent parameters [Eq. (5)], and thus can be inferred from experimental data.

A. Low frequency case

Equation (24) was used to obtain the quantity $I/[2mv^2(1+N)]$ from low frequency deflection experiments. As discussed in Sec. III B and shown in Fig. 4, the low frequency response is found to be independent of the applied field frequency, as expected from Eq. (6). The deflection is parabolic and proportional to the applied field strength.

B. Higher frequencies

As mentioned in Sec. III A, the angle that the arc axis makes with the electrode axis varies slowly. In order to account for this offset, this angle has been added to Eq. (9) as a third fit parameter,[24] θ,

$$\xi(z,t) = \frac{Mv}{\omega}\left[\cos\left(\tau - \frac{\omega z}{v}\right) - \cos(\tau) - \frac{z\omega}{v}\sin\left(\tau - \frac{\omega z}{v}\right)\right] + \theta z.\tag{40}$$

Data points $(z, \xi(z))$ are obtained from the camera images. The phase of the applied magnetic field, $\tau = \omega t$ at each image taken by the camera is known precisely from the phase of the current in the coils. Equation (40) is fitted to the data points with M, v, and angle θ as fit parameters using a nonlinear least-squares curve fit.[25]

The direction of Earth's magnetic field is transverse to the arc current, which puts a small parabolic deflection bias on the arc column. From the low frequency deflection data (Fig. 4), the maximum deflection occurs at the anode, and for the 0.4 Gauss Earth's magnetic field and a 4 cm long arc is $(0.015/\text{cm/Gauss})(0.4\ \text{Gauss})(4\ \text{cm})^2 = 0.1$ cm. This deflection is much smaller than the ≈ 1 cm arc column displacement due to the applied magnetic field and is neglected in the model.

Two example higher frequency fits to experimentally obtained arc shape are shown in Fig. 11. Such fits are obtained for many arc shapes for a range of frequencies, arc lengths, and arc currents, with the goodness of fit similar to the examples shown. The correlation coefficient R of the fits is plotted in Fig. 12 for several frequencies, and is generally 0.95 or higher, and typically is 0.98.

The jet speed v inferred from such fits is found to be is independent of frequency and amplitude of the applied mag-
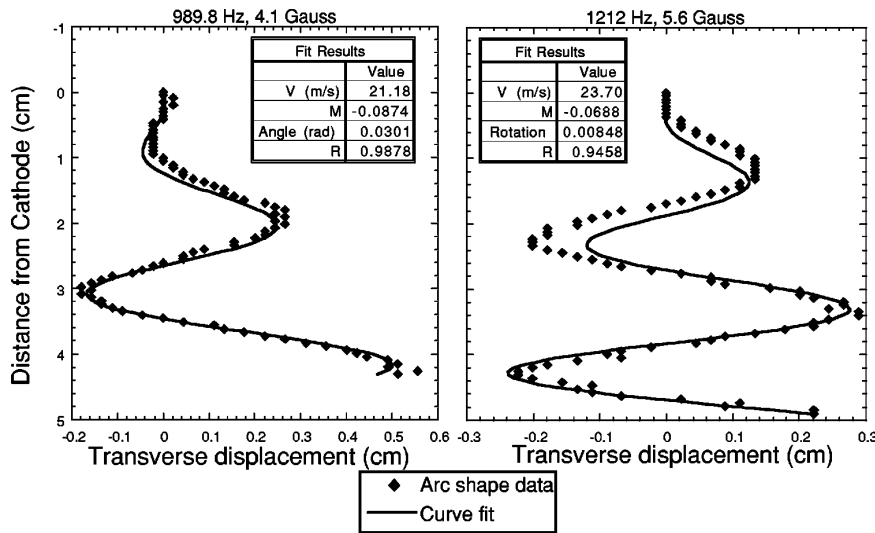
FIG. 11. Examples of experimentally obtained arc shape fitted by the model (neglecting the self-magnetic field effect). The jet speed v, interaction parameter M containing the mass density, and the angle of the arc axis are the fit parameters. R is the fit correlation coefficient. Horizontal scales are enlarged. Arc current is 150 A.

netic field to within the error bars, as can be seen in Figs. 13 and 14. This is as expected, since the jet speed is determined by the constriction at the cathode and should not depend on the applied field.[11] Its value is significantly below Maecker's estimate of ~ 200 m/s.[11] Maecker's estimate is that of the maximum jet velocity near to the cathode region, while the jet velocity inferred from the fits is an average along the arc length and cross section. Velocity profiles measured on similar arcs[26] show an initial rapid slowing down of axial flow within an arc diameter downstream of the cathode, due to momentum transfer to and entrainment of the surrounding gas,[26] followed by much a smaller gradient further down the axis.

The inferred jet speed is also seen to be independent of the arc length as length was varied by 30% (Figure 15). This indicates that at approximately 3 cm from the cathode, the gradient in the cross section averaged axial speed is smaller than the measurement error, i.e., $\partial v / \partial z \lesssim 5$ m/s/cm.

The value of the jet speed inferred from the fits is in agreement with speeds of particles observed moving in the arc using a fast framing camera.[27,28] These particles apparently come off the graphite cathode. An example is shown in Fig. 16. Particles were seen to traverse the length of the arc (≈ 4 cm) in 2 ms, giving a speed of ≈ 2000 cm/s. However, since the initial speed at which the particle is released from the cathode, and the amount of coupling of particle velocity to the gas flow has not been measured, it is not known how accurately the particle speeds represent the jet speed.

Having obtained the value of v from the high frequency fits, one can now quantify the low frequency limit $z\omega/v \ll 1$ derived in Sec. IV B. For a 4 cm long 150 A arc,

$$\omega \ll \frac{v}{z} \sim \frac{23 \, \text{m/s}}{0.04 \, \text{m}} = 575 \, \text{s}^{-1}. \tag{41}$$

Thus, the low frequency limit, and therefore parabolic deflection, should be obtained for frequencies $f \lesssim 575 \, \text{s}^{-1}/2\pi \sim 90$ Hz. As mentioned in Sec. III B, the deflection is parabolic for frequencies up to ≈ 80 Hz.

Figure 17 shows the variation of inferred jet speed with arc current. The jet speed scales linearly in this current range. This is in agreement with Maecker's scaling of jet speed[11] $v = \sqrt{(\mu_0/2\pi^2 r_c^2 \rho)} I$ if the cathode spot radius, r_c, remains constant.

Figure 18 shows the scaling of the fit parameter M with the applied field obtained from the high frequency fits. Since M determines the amplitude of the deflection and the arc shape is well fitted by Eq. (40), it can be inferred that the deflection amplitude is proportional to the applied field in this range of applied field amplitudes, as expected. The significance of the deviation of the value of M at the 0.8 G data point in the figure from the expected linear characteristic is not clear. The Earth's field is probably responsible for some of this deviation. However, the deflection due to the Earth's field is parabolic, and thus should not influence significantly the amplitude of the sinusoidal displacement for the 700 Hz data shown in the figure.

The mass density inferred from the fits exhibits fluctua-
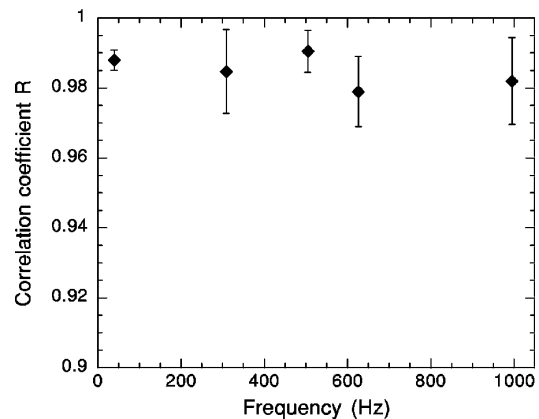
FIG. 12. Correlation coefficient R of the model fit to the arc shape for several frequencies of applied magnetic field.
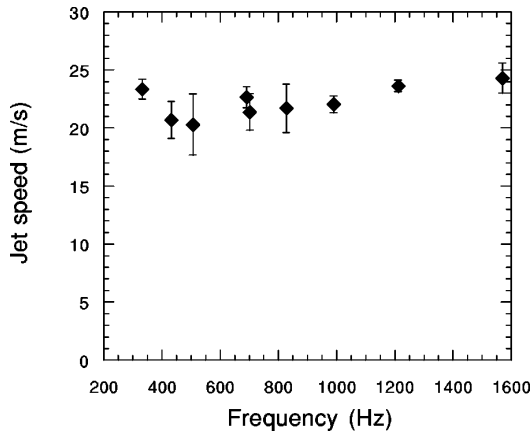
FIG. 13. Inferred jet speed is independent of the frequency of the applied magnetic field. Arc current is 150 A. Error bars are one standard deviation from measurements at different phases of magnetic field.

FIG. 15. Inferred jet speed is independent of arc length. Arc current is 150 A. Applied field frequency is 626 Hz. Error bars are one standard deviation from measurements at different phases of magnetic field.

tions from run-to-run, which are not explained by the model, as can be seen in Fig. 19. Based on measured temperature profiles of a 200 A carbon arc in air[29] and density values from Ref. 18, these linear mass density values imply an arc radius of approximately 0.7 cm, corresponding to a temperature at that radius of 6000–7000 K. Large radial temperature (and therefore, density) gradients at this arc radius could account for the variation of this parameter.

The density values at 20 Hz were obtained by assuming a jet speed of 23 m/s inferred from high frequency experiments and including the self-field effect as given by Eq. (24). It lies within the error bars of values at higher frequencies, indicating the model's consistency across this frequency range. Also shown is the value at 20 Hz if no self-magnetic field effect is included. The self-field effect is discussed in detail in Sec. V C below.

C. Self-field effects

In Sec. IV E, an attempt was made to include the effect of the self-magnetic field of the arc in the model by using an

analytical approximation resulting in a simplified self-field term in Eq. (21). This approximation gives an exponentially growing envelope for the arc shape for high frequencies, as discussed in Sec. IV E. In fact, the measured arc shapes do not show this exponential growth and the observed arc shape is best described by Eq. (5) without the simplified self-field term. This is illustrated in Fig. 20, in which the fit produced using Eq. (22) with the simplified self-field term is compared with the fit without this term. As can be seen in the figure, the model with the self-field approximation is only able to reproduce the first half-wavelength on the measured arc shape, and rapidly diverges from the arc shape with further distance from the cathode. Thus, it is found that including the self-field approximation of Eq. (21) gives an arc shape inconsistent with the observations. Therefore, for all the high frequency results presented above, arc shape was fitted using Eq. (5) neglecting self-field effect.

Several possible reasons why Eq. (22) fails to model the arc shape correctly are as follows. First, expression (17) for the force due to the self-magnetic field is a local approximation, neglecting the force due to the current in the rest of the arc column. Second, the expression is valid for $R \gg a$, where a is the arc radius. For higher frequency ac experiments, however, $R \sim a$. Thus, in order to properly take the self-field into account, a 2D model is needed, which would include a current density $J(x)$ instead of total current. Third, the ap-

FIG. 14. Inferred jet speed is independent of the applied field amplitude, as expected. Applied field frequency is 702.5 Hz; arc current is 150 A. Error bars are one standard deviation from measurements at different phases of magnetic field.
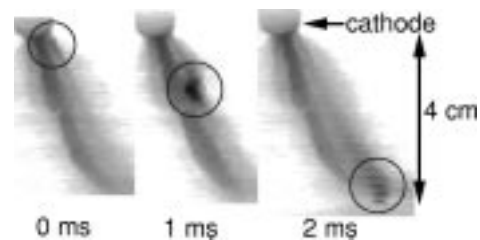
FIG. 16. Three consecutive frames showing the transit of a particle in the cathode jet. The camera framing rate was 1000 frames/s. The particle (circled) comes off the cathode at $t = 0$ ms and is seen to traverse the length of the arc (≈ 4 cm) in 2 ms, giving a speed of ≈ 2000 cm/s.
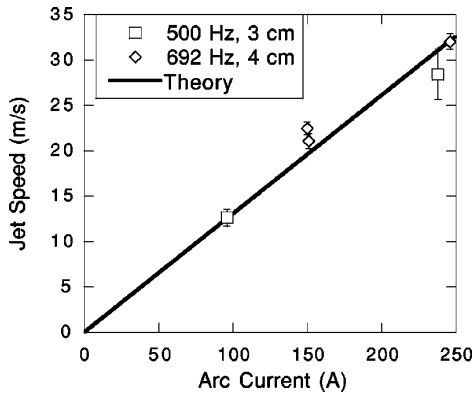
FIG. 17. Inferred jet speed scales linearly with the arc current. Applied field frequency is 500 Hz and 692 Hz and electrode separation is 3 cm and 4 cm, respectively. Error bars are one standard deviation from measurements at different phases of magnetic field.

proximation $1/R \approx \partial^2 \xi/\partial z^2$ is only good for $\partial \xi/\partial z \ll 1$, whereas $\partial \xi/\partial z$ approaches 1 in the high frequency experiments. Finally, an effect balancing the self-field force could be present that is not accounted for in the model. However, it is unlikely that such an effect could exactly cancel the self-field effect over the whole higher frequency (100–1600 Hz) and amplitude range of the present experiment.

A better approximation (still in the thin-wire approximation) of the self-magnetic field of the arc is calculated in the Appendix, in which the force due to self-field is integrated over the whole arc length. However, unlike the case of the simplified local analytical approximation discussed above, an analytical expression for the arc shape cannot be obtained in this case. Therefore, no fits to measured arc shape were possible in this case. The computed arc shape did not deviate significantly from the arc shape without the self-field term (Fig. 21), indicating that when integrated over the whole arc length, the self-field effect is small. A fully two-dimensional numerical calculation including the current density profile would be needed to fully resolve the issue.
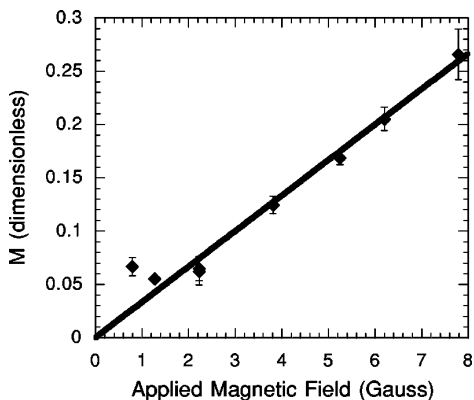
FIG. 18. Arc response is linear in the applied magnetic field. The applied field frequency is 702.5 Hz; electrode separation is 4 cm; arc current is 150 A. Error bars are one standard deviation from measurements at different phases of magnetic field.
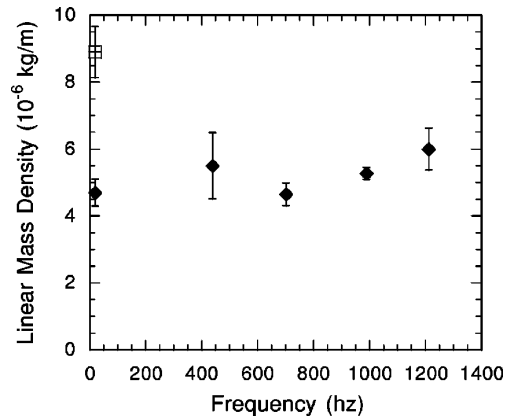
FIG. 19. Inferred linear mass density vs frequency of the applied magnetic field. Arc current is 150 A. The average jet speed $v = 23 \, m/s$ inferred from the high frequency fits was used to get mass density from the parabolic fits of the low frequency (20 Hz) data point, including the self-magnetic field. Also shown (as the open square point) is the value at 20 Hz if no self-magnetic field effect is included. Error bars are one standard deviation from measurements at different phases of magnetic field.

In the case of low frequency parabolic deflection, however, where the radius of curvature of the arc column is large, the local approximation should still apply. In fact, the more accurate approximation used in the Appendix reduces to the local approximation of Eq. (17) in the limit of parabolic deflection [Eq. (A4)], indicating that the self-field effect is significant in this case. That the self-field should reduce deflection for low frequencies, as predicted by Eq. (24) and seen in Fig. 19 can be seen as follows. For low frequency parabolic deflection, the curvature is pointing in the same direction as the arc displacement from the axis. For
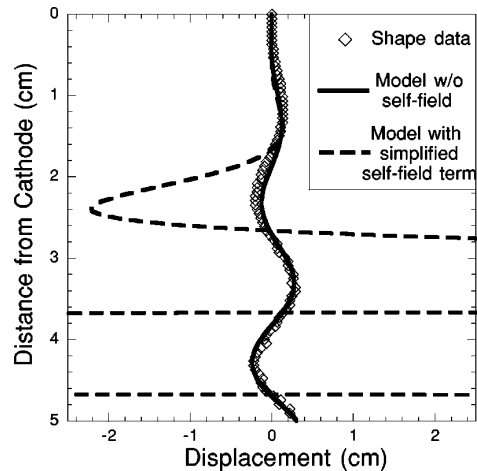
FIG. 20. Experimentally obtained arc shape fitted by the models with and without the simplified self-magnetic field term, shown with dashed and solid curves, respectively. The jet speed v and interaction parameter M containing the mass density are the fit parameters. The model with the simplified self-field term gives exponential growth of displacement amplitude and can only approximate the measured arc shape for the first half-wavelength of the displacement. Arc current is 150 A; applied magnetic field amplitude is 5.6 G; frequency is 1212 Hz.
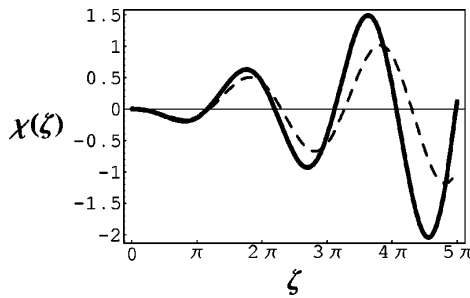
FIG. 21. Numerically calculated arc shape with the self-magnetic field effect. For comparison, the shape calculated without the self-field effect is shown as the dashed curve.

higher frequency sinusoidal displacement, however, the curvature is in the opposite direction to the displacement from the axis. The self-magnetic force is directed from the concave to the convex side of the bent current channel, tending to open the arc in the parabolic case, and thus decreasing the deflection, and tending to increase the bending in the sinusoidal case.

VI. AN INDUSTRIAL APPLICATION

In this section, the model used for fitting the arc deflection in the present experiment is applied to an industrial scale dc arc furnace. Because this involves extrapolation of almost three orders of magnitude in arc current, only an order of magnitude estimate will be attempted.

The typical values for a modern dc steelmaking arc furnace are[2] $I = 100$ kA, $v_{jet} \sim 1$ km/s, and furnace diameter $= 2r \sim 10$ m. The size of the furnace and the arc current imply a magnetic field at the arc from the wire feeds of $B \approx \mu_0 I / 2\pi r = 40$ G. Assuming an arc diameter of 10 cm and a mass density corresponding to air at 10 000 K of 1.7×10^{-2} kg/m³ gives linear mass density $m \sim 1 \times 10^{-4}$ kg/m. Using the model for dc arc deflection without the self-magnetic field [Eq. (6)], $\xi = (IB/2mv^2)z^2$, the deflection for 0.5 m long arc is 0.5 m at the anode, or $\approx 45°$ from the axis. This is similar to the deflection observed in some industrial furnaces,[8,9] before any power cable rerouting to decrease the stray magnetic fields.[7]

Equation (24) can be used to include the self-magnetic field effect. Using the above values, $N \approx 6$. This gives a deflection of only 0.07 m, or 8° from the axis. Thus, the self-field effect might play a significant role in stiffening the arc.

This simplified estimate neglects complexities arising from the irregularities in the geometry of unmelted scrap anode, of current distribution in the melt and the electrode, the effect of an iron furnace shell on the magnetic fields, and the effects of submerging the arc in a layer of foamy slag as done in steelmaking. Some of these effects are discussed in Refs. 2, 8, 30.

VII. DISCUSSION AND CONCLUSIONS

A systematic study was made of the behavior of the ≈ 150 A atmospheric pressure arc under the influence of dc and oscillating transverse magnetic fields. The experimental setup retains some of the features of industrial arc furnace and welding installations, i.e., the electrode geometry and materials, working gas composition and pressure, and the presence of transverse magnetic fields. The current range studied is similar to that utilized in welding.

A simple two-parameter model is proposed for the arc dynamics in transverse magnetic fields, based on a balance of $\mathbf{J} \times \mathbf{B}$ force and the inertia of the cathode jet. The model successfully describes the shape of the deflected arc for dc, low frequency, and high frequency magnetic fields, and gives reasonable values for the average jet speed v and the linear mass density m. Both of these parameters are found to be independent of the applied magnetic field characteristics, as expected. The inferred average jet speed scales linearly with the arc current, as predicted by the Maecker's model, but is an order of magnitude below the estimated peak value.

The simplicity of the model is also its limitation. The two free parameters v and m it requires are determined empirically from the experiments. No prescription is given for relating these to actual cross-sectional and axial profiles of velocity and mass density. Resolution of these issues would most likely require a 2D model with radial and axial profiles of the arc, including pressure, mass density, velocity, and current density, such as computed in Ref. 31 together with a closed set of MHD equations.

The self-magnetic field effect on the arc shape have not been successfully incorporated into the analytical description of the arc deflection at higher frequencies. As discussed in the Appendix, the self-magnetic field analysis breaks down at higher frequencies and has not been iterated to achieve self-consistency. However, the consistency of the model without the self-field effect with the experiment for the whole 100–1600 Hz frequency range indicates that self-field effects do not play a significant role in this parameter regime and that the local approximation used is inaccurate (Sec. V C). A numerical calculation of the self-field effect also supports this view (the Appendix).

The ability to use the thin-wire approximation to describe the arc dynamics in magnetic fields indicates the possibility of using this model to analyze instabilities in high current arcs such as those described in Ref. 32. Additionally, the importance of the cathode jet shown here indicates that it may play a role in determining stability properties as well.

In the above analysis, the average jet speed v and linear mass density m were determined from the application of a high frequency transverse magnetic field. This method may be applicable as a diagnostic of flow speed and density in other arcs and plasma torches where strong flows are present.

The model of the arc deflection presented here is directly applicable to the arc deflection in welding and also in material processing, where oscillating transverse magnetic fields have been used, for example, to spread the discharge over a wider processing area.[33] Although it involves a large extrapolation in arc current, the model gives a correct estimate for the deflection angle in steelmaking furnaces. However, an intermediate-scale (~ 10 kA) experiments should be performed to explore the applicability of the model to higher current regimes.

APPENDIX: FORCE DUE TO THE SELF-MAGNETIC FIELD OF THE ARC COLUMN

An expression for the force per unit length due to self-field for a plane curve $(z,\xi(z))$, for ξ small compared to the length scale of bending is given in Ref. 34,

$$F_{self} \approx \frac{\mu_0 I^2}{4\pi} \int \frac{(z-z')\frac{\partial \xi(z')}{\partial z'} - \xi(z) - \xi(z')}{[(z-z')^2 + a^2]^{3/2}} dz', \quad (A1)$$

where a is the arc radius. For a parabolically deflected arc, $\xi = Az^2$. Integrating Eq. (A1) from the cathode $z=0$ to the anode $z=h$, the force per unit length is

$$F_{self} = -\frac{\mu_0 I^2 A}{4\pi}\left\{ \ln\left(\frac{\sqrt{(h-z)^2 + a^2} + h - z}{\sqrt{z^2 + a^2} - z} \right) \right.$$
$$\left. - \frac{h-z}{\sqrt{(h-z)^2 + a^2}} - \frac{z}{\sqrt{z^2 + a^2}} \right\}. \quad (A2)$$

The maximum value of F_{self} is at $z=h/2$ and for $a/h \ll 1$ is equal to

$$F_{self,max} = -\frac{\mu_0 I^2 A}{4\pi}\left(2\ln\frac{h}{a} - 2 \right), \quad (A3)$$

where the minus sign indicates that the direction of the force is opposite to the deflection ξ, and is acting to decrease the deflection. The curvature for the parabola $\xi = Az^2$ is $1/R \approx -\xi''(z) = -2A$, for $\xi'(z) = 2Az \ll 1$, i.e., for $z \ll R$. Equation (A3) thus becomes

$$F_{self,max} = \frac{\mu_0 I^2}{4\pi R}\left(\ln\frac{h}{a} - 1 \right). \quad (A4)$$

Comparing the above to Eq. (17) and using the definition for N, we obtain that for low frequency and dc deflection,

$$N = \frac{\mu_0 I^2}{4\pi m v^2}\left(\ln\frac{h}{a} - 1 \right). \quad (A5)$$

For higher applied magnetic field frequencies, when the arc shape is not parabolic, integration in Eq. (A1) has to be done numerically. Substituting the arc shape derived neglecting the self-field effect [Eq. (9)] into Eq. (A1), the resulting F_{self} into Eq. (19), and solving the differential equation numerically, an approximate arc shape with the self-field effect can be obtained. Figure 21 compares the arc shape thus obtained with the one neglecting the self-field effect. A comparison with Fig. 10 shows that the analytic form [Eq. (17)]

gives an overestimate of the self-field effect. The arc shape in Fig. 21 is still an approximation, however, since the self-field force obtained is not self-consistent and the process needs to be iterated. Also, Eq. (A1) starts to break down as $\chi(\zeta)$ approaches the wavelength of the bending.

[1] P. Fauchais and A. Vardelle, IEEE Trans. Plasma Sci. **25**, 1258 (1997).
[2] B. Bowman, in *Electric Furnace Conference Proceedings, Nashville, 1994* (Iron and Steel Society, Warrandale 1995), Vol. 52, p. 111.
[3] *The Physics of Welding*, edited by J. F. Lancaster, 2nd ed. (Pergamon, New York, 1986).
[4] E. Pfender, in *Gaseous Electronics*, edited by M. N. Hirsh and H. J. Oskam (Academic, New York, 1978), Vol. I, Chap. 5.
[5] T. W. Myers and W. C. Roman, ''Survey of Investigations of Electric Arc Interactions with Magnetic and Aerodynamic Fields,'' Technical Report ARL No. 66-0184, Aerospace Research Labs, Wright-Patterson Airforce Base, 1966, see National Technical Information Service Document No. 19670015507 N (67N24836), NTIS No. AD-646752. Copies may be ordered from the National Technical Information Service, Springfield, Virginia 22161.
[6] G. R. Jones, *High Pressure Arcs in Industrial Devices: Diagnostic and Monitoring Techniques* (Cambridge University, Cambridge, 1988).
[7] N. Ao and M. Nakai, SEAISI Q. , 20 (1994).
[8] B. Bowman and F. Fitzgerald, J. Iron Steel Inst. **211**, 178 (1973).
[9] M. Sharifi, Master's thesis, University of Toronto, 1994.
[10] H. Maecker, Proc. IEEE **59**, 439 (1971).
[11] H. Maecker, Z. Phys. **141**, 198 (1955); E. Pfender, in *Gaseous Electronics*, edited by M. N. Hirsh and H. J. Oskam (Academic, New York, 1978), Vol. I, Chap. 5, pp. 338–339; P. M. Bellan, Phys. Rev. Lett. **69**, 3515 (1992).
[12] K. Bartels and J. Uhlenbusch, Z. Angew. Phys. **29**, 122 (1970); J. Uhlenbusch, Physica (Utrecht) **82**C, 61 (1976).
[13] Z.-Y. Guo, Int. J. Heat Mass Transf. **27**, 383 (1983).
[14] G. Speckhofer and H. P. Schmidt, IEEE Trans. Plasma Sci. **24**, 1239 (1996).
[15] G. B. Serdyuk, Automatic Welding **13**, 26 (1960).
[16] M. Karasik and S. J. Zweben, ''Experiments and modeling of an instability of an atmospheric pressure arc,'' Phys. Plasmas (submitted).
[17] H. Maecker and H. G. Stablein, IEEE Trans. Plasma Sci. **PS-14**, 291 (1986).
[18] M. I. Boulos, P. Fauchais, and E. Pfender, *Thermal Plasmas: Fundamentals and Applications* (Plenum, New York, 1994), Vol. I.
[19] D. J. Tritton, *Physical Fluid Dynamics*, 2nd ed. (Oxford University Press, New York, 1988).
[20] A. Jeffrey and T. Taniuti, *Magnetohydrodynamic Stability and Thermonuclear Containment* (Academic, New York, 1966).
[21] F. B. Hildebrand, *Advanced Calculus for Applications* (Prentice–Hall, Englewood Cliffs, 1962).
[22] J. P. Friedberg, *Ideal Magnetohydrodynamics* (Plenum, New York, 1987).
[23] D. Book, NRL Plasma Formulary, Naval Research Lab, 1990.
[24] Strictly speaking, this parameter is the slope of the arc axis with respect to the electrode axis, i.e., slope=$\tan(\theta)$, where θ is the angle between the two. However, since $\theta \ll 1$, $\tan(\theta) \approx \theta$.
[25] Abelbeck Software, KaleidaGraph™, Software package, Version 3.0.1, Reading, 1993.
[26] E. Pfender, J. Fincke, and R. Spores, Plasma Chem. Plasma Process. **11**, 529 (1991).
[27] Courtesy of Glen Wurden, Los Alamos National Laboratory, Los Alamos, New Mexico.
[28] R. J. Maqueda and G. A. Wurden, Nucl. Fusion **39**, 629 (1999).
[29] Y. P. Raizer, *Gas Discharge Physics* (Springer-Verlag, New York, 1991).
[30] J. C. Borrel, L. Mineau, N. Meysoson, and J. L. Roth, La Revue de Metallurgie—CIT **93**, 497 (1996).
[31] J. W. McKelliget and J. Szekely, J. Phys. D **16**, 1007 (1983).
[32] R. W. Montgomery and C. M. H. Sharp, Br. J. Appl. Phys., J. Phys. D **2**(2), 1345 (1969).
[33] V. F. Put'ko, in *Thermal Plasma and New Materials Technology*, edited by O. P. Solonenko and M. F. Zhukov (Cambridge Interscience Publishing, Cambridge, 1994), Vol. 1, pp. 229–249.
[34] W. B. Thompson, *An Introduction to Plasma Physics* (Pergamon, New York, 1962).